Earth and Planetary Science Letters 452 (2016) 133–145

Contents lists available at ScienceDirect

Earth and Planetary Science Letters

www.elsevier.com/locate/epsl

# Hidden secrets of deformation: Impact-induced compaction within a CV chondrite

L.V. Forman [a,*], P.A. Bland [a], N.E. Timms [a], G.S. Collins [b], T.M. Davison [b], F.J. Ciesla [c], G.K. Benedix [a], L. Daly [a], P.W. Trimby [d], L. Yang [d], S.P. Ringer [e]

[a] Department of Applied Geology, Curtin University, GPO Box U1987, Perth, WA 6845, Australia
[b] Royal School of Mines, Department of Earth Science & Engineering, Imperial College London, Prince Consort Road, South Kensington, SW7 2BJ, United Kingdom
[c] Department of the Geophysical Sciences, The University of Chicago, 5734 South Ellis Avenue, Chicago, IL 60637, USA
[d] Australian Centre for Microscopy and Microanalysis, The University of Sydney, NSW, 2006, Australia
[e] Australian Institute for Nanoscale Science and Technology, and School of Aerospace, Mechanical and Mechatronic Engineering, The University of Sydney, NSW, 2006, Australia

ARTICLE INFO

*Article history:*
Received 1 October 2015
Received in revised form 27 July 2016
Accepted 27 July 2016
Available online 12 August 2016
Editor: C. Sotin

*Keywords:*
Allende
impact
compaction
meteorite
deformation
crystallography

ABSTRACT

The CV3 Allende is one of the most extensively studied meteorites in worldwide collections. It is currently classified as S1—essentially unshocked—using the classification scheme of Stöffler et al. (1991), however recent modelling suggests the low porosity observed in Allende indicates the body should have undergone compaction-related deformation. In this study, we detail previously undetected evidence of impact through use of Electron Backscatter Diffraction mapping to identify deformation microstructures in chondrules, AOAs and matrix grains. Our results demonstrate that forsterite-rich chondrules commonly preserve crystal-plastic microstructures (particularly at their margins); that low-angle boundaries in deformed matrix grains of olivine have a preferred orientation; and that disparities in deformation occur between chondrules, surrounding and non-adjacent matrix grains. We find heterogeneous compaction effects present throughout the matrix, consistent with a highly porous initial material. Given the spatial distribution of these crystal-plastic deformation microstructures, we suggest that this is evidence that Allende has undergone impact-induced compaction from an initially heterogeneous and porous parent body. We suggest that current shock classifications (Stöffler et al., 1991) relying upon data from chondrule interiors do not constrain the complete shock history of a sample.

© 2016 The Authors. Published by Elsevier B.V. This is an open access article under the CC BY license (http://creativecommons.org/licenses/by/4.0/).

## 1. Introduction

Planetary systems evolve from a molecular cloud comprised of dust (condensed minerals and presolar grains) and gas, to a protoplanetary disk, where most of the mass is concentrated in the 'mid-plane' of that disk. Turbulence allows for gas and particle clumping and accretion of the dust into centimetre- to metre-sized bodies (Cuzzi and Weidenschilling, 2006). Interactions with the gas and collisions lead these solids to grow and accumulate into planetesimals measuring 10 s to 100 s of kilometers in diameter. As this accumulation must be relatively gentle to ensure sticking and adhesion among the components, primordial planetesimals formed in this way would preserve large pore spaces in between each component, resulting in very high porosities (>65%) (Blum, 2003; Weidenschilling and Cuzzi, 2006).

Planetary evolution from these primordial objects to the asteroids that we see today requires that porosity be greatly reduced, as evidenced by the worldwide collection of meteorites that comprises comparatively low-porosity rocks. A number of mechanisms for porosity reduction and weak fabric development have been suggested, including metamorphism and expansion/contraction cycles (Stacey et al., 1961; Zolensky et al., 1997), accretional compaction (Cain et al., 1986), gravitational compaction (Fujimara et al., 1983) and sedimentation; perhaps the two most plausible mechanisms being compaction from lithostatic overburden (Cain et al., 1986) and impacts (Scott, 2002; Sharp and DeCarli, 2006; Davison et al., 2010; Beitz et al., 2013; Bland et al., 2014). It is apparent that the gravity field of even relatively large planetesimals would be insufficient and to generate the required lithostatic pressure to cause sufficient compaction that could adequately explain the low porosities of meteorites (Weidenschilling and Cuzzi, 2006; Friedrich et al., 2014). The anisotropy of magnetic susceptibility (AMS) studies done by Gattacceca et al. (2005) conclude that dynamic compaction via impacts is the most likely mechanism for

* Corresponding author.
*E-mail address:* lucy.forman@curtin.edu.au (L.V. Forman).

http://dx.doi.org/10.1016/j.epsl.2016.07.050
0012-821X/© 2016 The Authors. Published by Elsevier B.V. This is an open access article under the CC BY license (http://creativecommons.org/licenses/by/4.0/).

fabric development and therefore porosity reduction, which is also supported by a wide number of findings within meteorite collections; low (but variable) porosities throughout a given sample; heterogeneous porosities within the same chondrite group; subtle mineral deformation microstructures; widespread planar fabrics; and localised melt pockets within matrix (Nakamura et al., 1992; Consolmagno et al., 1998; Brenker et al., 2000; Cuzzi et al., 2008; Johansen et al., 2009). Such evidence is not unique to carbonaceous chondrites; it is also present in ordinary chondrites, in the form of high-pressure polymorphism, vitrification of silicate minerals and deformation of olivine grains (Rubin, 2004). Recent work on the CM meteorite Murchison has also revealed porosity loss was induced by impact and predicted a pre-compaction bulk porosity of up to ∼50% (Hanna et al., 2015). Further support for the occurrence of impacts on early highly porous bodies is found in Housen et al.'s work (1999) regarding impact-cratering on the asteroid Mathilde; an unusual lack of blanket ejecta around prominent craters indicate the impacts that produced them occurred when the body was highly porous. Other studies also argue that impacts on such a large scale may destroy the target body if the porosity was not sufficiently high and the impact direct; the pores allow the target to sustain the impacts without being disrupted and oblique impacts lead to less ejecta and the crater morphologies present on Mathilde (Housen et al., 1999; Cheng and Barnouin-Jha, 1999; Housen and Holsapple, 2011). Impact-induced compaction is therefore discussed in depth with relation to the research outlined in this paper.

Evidence of impact shock is routinely observed in current meteorite collections and a shock level is assigned to each meteorite (Stöffler et al., 1991; Scott et al., 1992; Sharp and DeCarli, 2006). The approach taken by Stöffler et al. (1991) uses published data from impact experiments on low-porosity and homogeneous terrestrial rocks, lunar rocks and single crystals, taking these materials as analogues for low-porosity, H, L and LL ordinary chondrites. A set of shock metamorphic features seen in analogue materials are used to calibrate the peak pressure experienced for that meteorite, and determine a shock level. This classification is based upon the largest of grains in any sample (Stöffler et al., 1991; Scott et al., 1992), meaning only a few larger grains are considered. Allende, the sample of study in this paper, is identified as an S1-virtually unshocked- and is expected to have experienced no more than 5 GPa in peak shock pressure (Scott et al., 1992). The samples and procedures used in the early study may not be ideal for several reasons: meteorites are not homogeneous materials, and grain size plays an important role in determining the shock reaction of a grain, especially when pore space is considered (Davison et al., 2010). Most importantly, the experimental impact studies that underpin the Stöffler et al. (1991) and Scott et al. (1992) approach are concerned with impacts into low- or zero-porosity targets and, by extension, impacts into compacted planetesimals. Therefore, this approach may not be suitable for approximating impacts into highly porous primordial objects.

Recent numerical models consider more complex scenarios, concerned with impacts into uncompacted porous planetesimals, bimodal material and mixed compositions of the target body. Davison et al. (2010) model shock propagation through homogeneous, porous planetesimals and find high porosity to be positively related to higher impact-generated temperatures on an asteroidal scale. Similar numerical simulations have highlighted the importance of pore collapse in the target body upon impact, which generates large amounts of heat, allowing the whole medium to experience elevated temperatures and potential melting (Consolmagno et al., 1998; Davison et al., 2010; 2014). Further improvements were made to these models to acknowledge the small-scale and complex material properties of primitive bodies: chondrites are essentially bimodal mixtures of porous, fine-grained matrix and large chondrules without intercrystalline porosity (Bland et al., 2011; 2014; Davison et al., 2014). In an impact compaction simulation with a bulk shock pressure of only ∼1 GPa, the bulk post-shock temperature was ≈ 425 K, but the matrix was heated to ≈ 530 K from an initial temperature of 300 K, whereas chondrules were heated by only a few degrees (Bland et al., 2014). Heating occurs at chondrule edges adjacent to initially porous areas of matrix, and at the edges of closely spaced chondrules, and pressure distribution within chondrules is also not uniform; chondrule edges are predicted to experience higher pressures than chondrule interiors. Porosity in matrix also varies, with high-porosity regions observed in the lee of chondrules. Petrologic evidence of these features has yet to be identified, but the models give an indication of how a bimodal heterogeneous material may react upon impact.

In light of the models described above (Davison et al., 2010; Bland et al., 2014), the shock pressure aspect of Allende's impact history may simply be absent from large, resilient chondrules. Allende is a well-studied sample that contains approximately 40% matrix (Macke et al., 2011), and has a measured bulk porosity of 22%. Recent fabric analysis has inferred that ∼50% pore volume reduction has occurred in Allende via impact (Bland et al., 2011; Hanna et al., 2015), but this is unlikely to be homogeneous throughout any sample. Assuming initial matrix porosity in the >65% range, this implies a pre-compaction matrix:chondrule volume ratio of $> 2:1$. Numerical simulations that exposed such a chondrule–matrix mixture to a ∼1 GPa shock wave reproduced the observed bulk and matrix porosity in Allende, and suggest that localised heating by heterogeneous pore collapse may have been a significant process.

In this study we explore the possibility that matrix grains and chondrules responded differently to planetary compaction. We establish how the microanalytical and textural study of this meteorite holds interesting implications about the evolution of the parent body of Allende.

## 2. Approach & methods

In this study we analysed a thin section of Allende. The initial imaging of this sample was conducted at the X-Ray Fluorescence Beamline (XRF) at the Australian Synchrotron facilities in Melbourne. Here, 25 element maps were collected for the entire sample in under 10 h (Fig. 1). These were compared with the collected Energy Dispersive Spectroscopy (EDS) data for accuracy of elemental distribution throughout the sample, in addition to monitoring any instrumental drift. The Maia detector on this beamline had an energy sensitivity in the range of 3.3–19.9 keV, encompassed a number of major elements with an energy resolution of 300–400 eV, and in this case, produced maps with a spatial resolution of 2 µm per pixel. Elements were detected in the spectra processing stage and so were not required beforehand for the imaging to occur. In addition, the Maia detector was able to detect elements at the 10–100 ppm scale – commonly lower than other traditional imaging techniques (Fisher et al., 2014). Owing to the high-energy beam in use (18.5 keV), this technique sampled a larger depth than other traditional imaging techniques, and so data collected represented an average of the volume sampled (Dyl et al., 2014). Further information regarding this imaging technique can be found in the Analytical Methods section of Dyl et al. (2014). This map was used as a means of identifying areas of interest for further Secondary Electron (SE), Backscatter Electron (BSE), EDS and Electron Backscatter Diffraction (EBSD) analyses.

Ten regions encompassing chondrules, Amoeboid Olivine Aggregates (AOAs) and matrix grains were mapped using a variety of imaging techniques, utilising the Tescan Mira3 FESEM, at the John de Laeter centre at Curtin University, Western Australia. It is important to note that all maps were taken in the same physical

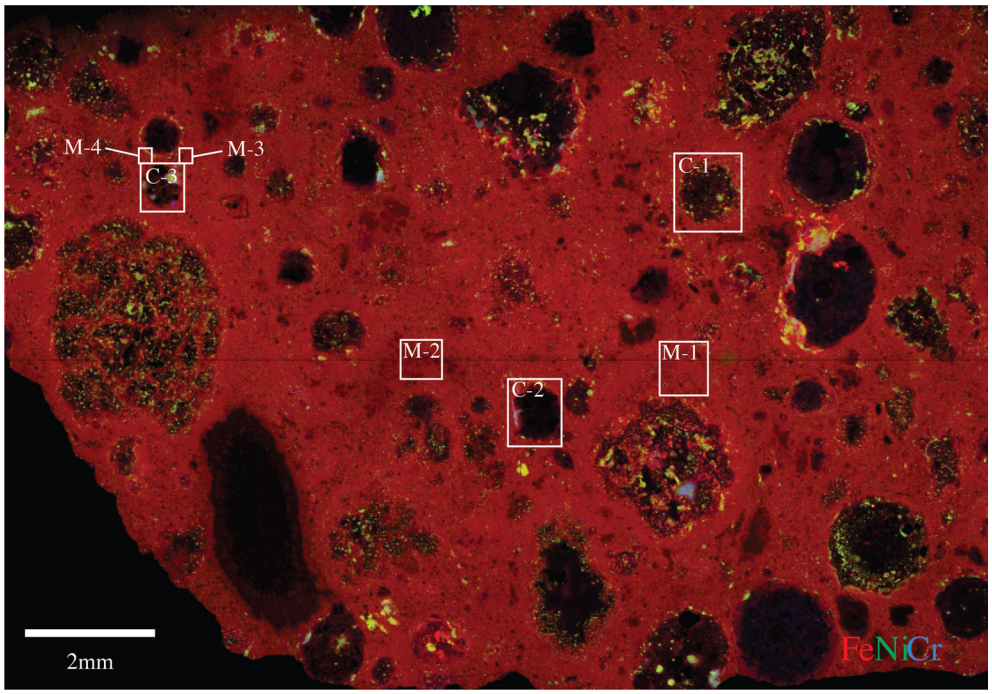


**Fig. 1.** X-Ray Flourescence Synchrotron map of a thin section of the Allende meteorite. Chondrule and matrix sites to be discussed are shown (C = chondrule/AOA, M = matrix). Note that M-1, M-3 and M-4 are proximal to a chondrule or AOA, and M-2 is in an area devoid of chondrules, AOAs and CAIs.

**Table 1**
EBSD and SEM imaging parameters used for imaging at each of the chondrule, AOA and matrix sites in this sample of Allende.

| Site | Type | Step size (μm) | Imaging threshold (μm) | Number of points | Mean Angular Deviation (MAD) (°) | Acc. voltage (keV) | Forsterite indexed (%) | Not indexed (%) |
|---|---|---|---|---|---|---|---|---|
| C-1 | Chondrule | 0.5 | 2 | 77284 | 0.38 | 20 | 82.5 | 16.0 |
| C-2 | Chondrule | 2 | 8 | 172125 | 0.60 | | 45.8 | 49.8 |
| C-3 | AOA | 0.81 | 3.6 | 2403310 | 0.53 | | 36.3 | 63.2 |
| M-1 | Matrix | 0.1 | 0.4 | 130732 | 0.68 | | 48.9 | 49.0 |
| M-2 | Matrix | 0.12 | 0.48 | 2314956 | 0.67 | | 37.2 | 59.3 |
| M-3 | Matrix | 0.2 | 0.8 | 122760 | 0.67 | | 36.55 | 52.87 |
| M-4 | Matrix | 0.35 | 1.4 | 35708 | 0.80 | | 37.9 | 57.1 |

orientation in the SEM, allowing for direct and accurate comparisons of crystallographic features between sites.

Standard Secondary Electron (SE) and Back-Scattered Electron (BSE) images were collected at a voltage of 20 keV, a beam intensity of 17, an aperture size of 30 μm and a working distance between 10 and 15 mm. These images were used to define regions of interest for further analysis and image collection.

Electron Backscatter Diffraction (EBSD) was the primary technique used in the study. EBSD enabled mapping of the crystallographic orientation of grains in a thin section, both in relation to crystallographic axes and neighbouring grains. Automated and simultaneous EBSD and EDS maps were generated using Oxford Instruments' Aztec acquisition system, using a fixed $x$ and $y$ step size for each site in a user-defined grid, varying between 0.1 μm and 8 μm, dependant upon the grain size distribution at each particular site. This approach generated a dataset with high spatial resolution whilst also being time-efficient. Table 1 shows the conditions under which the maps were collected at each site. SE images were obtained to confirm that topographic features present in or around chondrules did not bias the EBSD data and interpretation.

Allende was found to contain abundant matrix grains at the sub-micrometre scale, and so greater spatial resolution was required for accurate analysis of the smaller grains. The Transmission Kikuchi Diffraction (TKD) technique utilised electron transparent samples in the SEM, coupled with conventional EBSD instrumentation, resulting in an order of magnitude improvement in spatial resolution compared to EBSD (sub 10 nm – Trimby et al., 2014). A transmission electron microscope (TEM) foil was extracted containing a sectional view of a chondrule rim and adjacent matrix material. The sample was created using a focused ion beam (FIB) SEM (Carl Zeiss Auriga) at the Australian Centre for Microscopy & Microanalysis (ACMM), Sydney. To protect the sample from gallium beam damage a platinum layer was deposited and the sample lifted out using a Kleindiek micromanipulator. The section was mounted on a molybdenum grid using platinum welds and the sample was further thinned to 100 nm. The TEM foil was analysed using TKD and EDS on a Carl Zeiss Ultra Plus FEG SEM at the ACMM, Sydney. TKD and EDS data were acquired using an Oxford Instruments AZtec system with a Nordlys-Nano EBSD detector and an X-Max 20 $mm^2$ SDD EDS detector and with an accelerating voltage of 30 kV.

EBSD data were processed using the Oxford Instruments HKL software package Channel 5.12, generating crystallographic orientation maps, phase maps and pole figure plots that were compared across each site. In this process, noise reduction and data processing were done in a very similar manner to that described in Watt et al. (2006); isolated misindexed data points were removed using a wildspike correction, and all non-indexed points infilled to a six nearest-neighbour extrapolation. Grains were detected in each map based upon crystallographic orientation, and using a misori-

entation angle of at least 10° between two adjacent pixels to identify grain boundaries. Grains with diameters less than four times the step size were removed to allow for reliable data interpretation, which also removed misindexed points. Grain orientation data from the entirety of each map were plotted on to lower hemisphere, equal area projections as one point per grain to avoid grain size related bias during contouring. In this study, we focused on olivine grains to enable a direct comparison with shock-level studies. Although compositions across the olivine solid-solution can be found in Allende, there was little variation in their crystal structure: EBSD does not discriminate between olivine sub-types, and so all EBSD patterns from olivine were successfully indexed using the 'forsterite' match unit in the HKL database (indexing statistics are given for each region of interest in Table 1).

Low-angle boundaries (LABs) can form due to a number of mechanisms. Both orientation selective dissolution and grain growth in a vein setting may result in grains of similar orientation forming apparent low-angle sub-grain boundaries where their edges meet. Neither of these mechanisms are likely given the primitive nature of Allende. LABs can also be a geometric consequence of grain impingement between two similarly-orientated grains (Wheeler et al., 2001). Where grains preserve crystallographic variations that cannot be attributed to fractures, it was assumed that they were deformed crystal-plastically (via dislocation creep and recovery). Dislocation slip systems were then inferred assuming pure tilt boundary geometry, whereby an orthogonal relationship exists between the rotation axis of low-angle boundaries, pole to the dominant dislocation slip plane and slip direction (e.g. Prior et al.) combined with cumulative dispersion of crystallographic poles in each grain. As the rotation axes did not lie in the plane perpendicular to the LAB trace, we can infer these boundaries formed due to tilt and did not show evidence of twist-boundary formation. Further information regarding this test can be found in the methods section of Gray (2013). LAB planes were inferred from traces in map view and contain misorientation axes. Axes of misorientation were identified based upon axes of pole dispersions in lower hemisphere plots. The related slip systems were then inferred using geometric criteria: a slip-system is composed of both a slip plane and direction; the pole to the slip plane is contained within the low-angle boundary with the misorientation axis, and the slip direction is perpendicular to that plane.

The numerical simulations described by Bland et al. (2014) provided peak and post-shock stress (pressure), temperature and porosity distributions for numerous impactor velocity and initial matrix/chondrule abundance scenarios. To compare more directly the data from our study with the simulation predictions, shear strain distribution maps were produced from the simulation outputs. The tracer particle positions in the simulations were used to derive the second invariant of the total strain tensor using the method described by Bowling (2015). This invariant measure of shear deformation includes the net elastic plus plastic strain at the end of the simulations (i.e., the finite strains). As the elastic–plastic rheological model used in the numerical simulations to represent the chondrules and matrix incorporates a yield strength that is pressure, strain and temperature dependent, it can describe (very approximately) both brittle (low pressure) and ductile (high pressure) deformation. In reality, olivine rheology is more complex in detail, and involves anisotropic elastic and plastic properties. Furthermore, as the matrix of fine grains and interstitial pore space is treated as a uniform continuum in the simulations, we note that the strain in the matrix is the bulk strain of the grains and the pore spaces, which will be largely accommodated by grain rearrangement and pore collapse, rather than permanent deformation of individual matrix grains: i.e., 'details' of the strain in individual matrix grains is not resolved. Despite these limitations we expect the qualitative distribution of shear strain observed in the numerical simulations to provide an informative comparison with permanent strain derived from our crystallographic orientation analysis.

## 3. Results & analysis

Olivine in the chondrules in Allende was commonly Mg-rich, i.e., forsteritic, whereas matrix olivine was more Fe-rich, i.e., fayalitic (Fig. 1). Prior studies calculate proportions of chondrule and matrix to be approximately 60% and 40% respectively (McSween, 1979; Macke et al., 2011). The chondrules, AOAs and Calcium–Aluminium Inclusions (CAIs) were also weakly elongate as is shown in Fig. 1. Within the 1.28 $cm^2$ sample area of our sample, we observed a large variation in matrix grain size (Supplementary Figs. 1–4). EBSD analyses resolved forsterite, diopside, and enstatite, which have been recorded previously (Stöffler et al., 1991). As expected, this sample was highly texturally heterogeneous, containing different chondrule types and a wide range of matrix grain shapes and sizes. We found no evidence of high-pressure polymorphs, such as ringwoodite, that would indicate high shock pressures.

### 3.1. Chondrules and AOAs

Three chondrule and AOA sites were examined (Fig. 2), and are collectively referred to as 'chondrule sites' from this point forward. For each site, a 'cumulative misorientation map' was generated such that each datapoint was coloured for the minimum mismatch in crystallographic orientation (minimum misorientation) from a user-specified point within the grain (all sites, Fig. 2c). These maps resolved misorientations to a precision based upon the fit quality of the indexing solutions (mean angular deviation (MAD), Table 1) in each map, which were typically reliable down to approximately 0.5° in this study. Each of the chondrules showed very little or no internal deformation in their interior: up to a maximum of 1° in the central parts of the grains. However, the outer 10–30 μm of the chondrule and outermost AOA grains commonly preserved up to 6° of progressive, cumulative misorientation that did not relate to brittle fractures (all sites, Fig. 2c and Fig. 3). This relationship is visible in the local misorientation maps, where each pixel was coloured to reflect mean misorientation with the eight nearest neighbour data points (Fig. 4). Figs. 3 and 4 show that progressive crystallographic misorientations at the edges of the grains are accommodated by many relatively planar LABs, parallel to the grain edge. Fig. 3 demonstrates the deformation at C-1 is cumulative and begins in the outer 30 μm of the grain, reaching maximum deformation at the edge (7–8°). Not only were the highest degrees of strain at the grain edges at each site, but LABs were also generally concentrated at the top and bottom, and to the right of the chondrules and AOA, as indicated by the continuous, cumulative strain at the margins of chondrule C-1, for example (Figs. 2b, 2c, 3 and 4).

### 3.2. Matrix grains

Maps of crystallographic orientation for olivine at the four matrix sites are shown in Fig. 5. Grain size and shape maps and distribution histograms are presented in Supplementary Figs. 1–4, and matrix grains measured in the TKD section are shown in Fig. 6. It is clear a variety of grain sizes are present; between 0.1 μm and 50 μm. The grains were chiefly subhedral and lath-shaped, characterised as having an aspect ratio greater than 2:1 in 2D. A wide range of intragrain misorientation characteristics were observed at a very fine scale in matrix grains; up to 20° of internal deformation across a 20 μm grain was recorded at site M-2, with as little

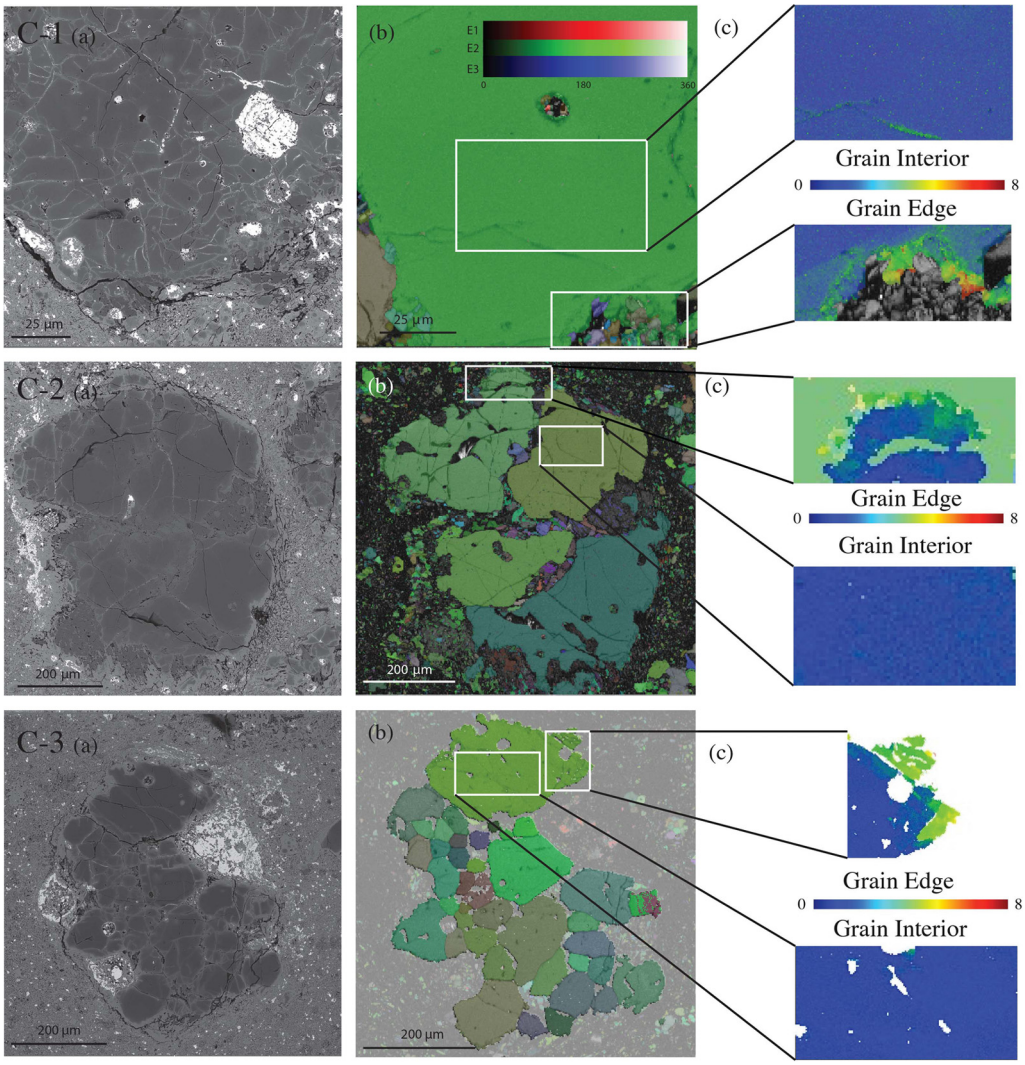


**Fig. 2.** Chondrule/AOA sites C-1, C-2 and C-3 respectively. (a) Backscatter Electron (BSE) images, (b) Euler maps of each site, showing the orientation of each grain in terms of the three Euler angles, and (c) texture component maps showing a vast increase in deformation at grain edges when compared to grain interiors (scale bar is shown in degrees °).

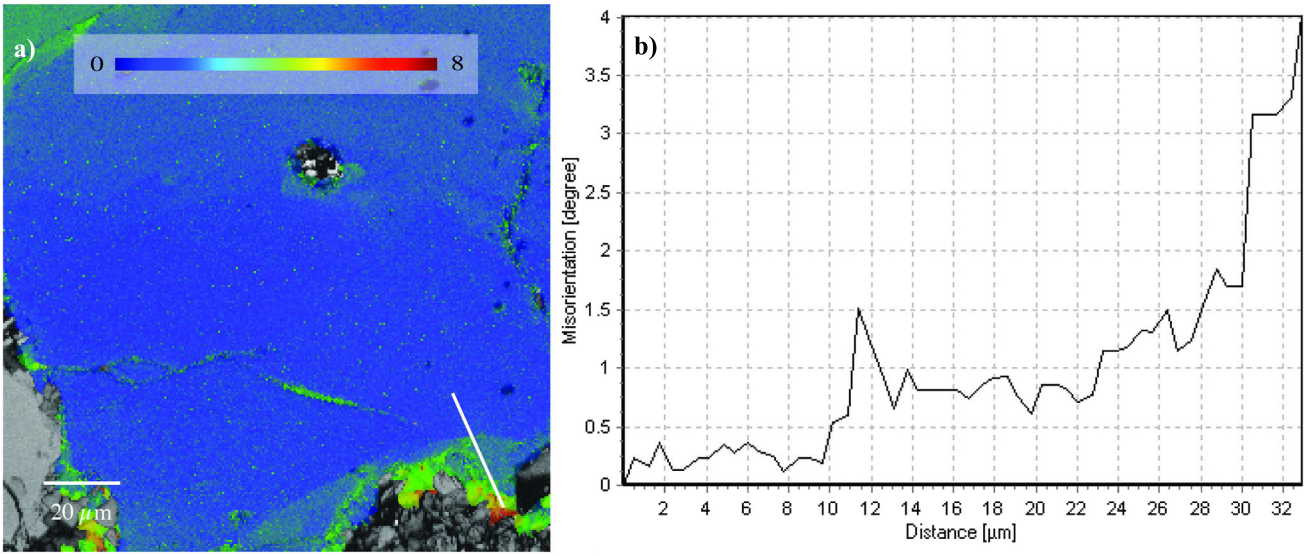


**Fig. 3.** (a) Map of texture component for chondrule at C-1. White transect line is shown through lower outer edge of the chondrule. (b) Misorientation profile for the white transect line in (a) demonstrates the gradual increase in orientation deviation in an outwards direction from the innermost point of the transect. This confirms the outer edges of chondrules deform gradually and cumulatively from the inner to outer points along the transect.

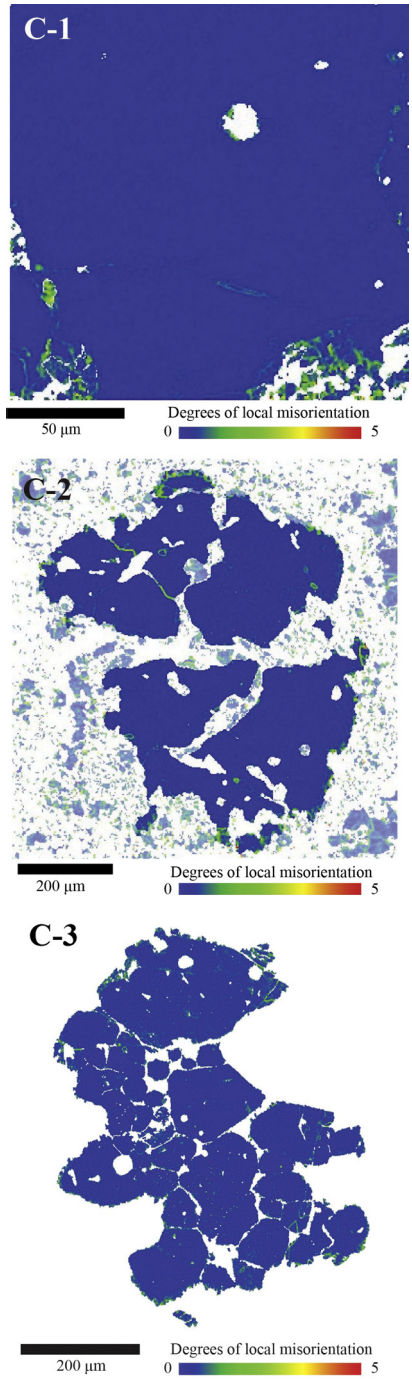


**Fig. 4.** Local misorientation maps of the chondrule/AOA sites. Each pixel is colour coded to reflect its degree of misorientation from the surrounding 8 pixels.

as 2° internal deformation across a selection of grains at site M-1 (Figs. 5 and 6). Whilst a wide range of values were recorded, average internal deformation was high, with the majority of values in the 8–15° range. It is important to note that in contrast to chondrules, intragrain deformation was observed throughout the full length of the matrix grains, and the magnitude of deformation is consistently greater in all cases.

At sites M-1 and M-3, the trace of planar LAB orientations were measured relative to the map $x$–$y$ reference frame plotted onto rose diagrams (Fig. 7). The rose plots reveal a dominant trend of the LABs, preferentially aligned with map $y$ direction (i.e., circa 0° and 180° in Fig. 7). This is significant because aligned LABs indicate a relatively consistent applied stress field at the scale of the observations, such as those produced in controlled olivine deformation experiments by Kohlstedt and Goetze (1974). The spatial density of low-angle boundaries was more consistent throughout the matrix grains when compared with chondrule sites; where chondrules and AOAs have a higher density of LABs at their edges, those found in matrix grains were not confined to the grain edges and were present throughout the grain area (Figs. 5 and 6). This is consistent with findings of experimentally stressed olivine crystals; undulose extinction along the grains indicates multiple, similarly oriented low-angle boundaries are present, accommodating changes in crystallographic orientation (Kohlstedt and Goetze, 1974; Fliervoet et al., 1999).

The matrix sites also presented a range of porosities. In some locations, grains appeared very compact with an extremely low porosity (e.g. M-2), whereas areas of M-1 and M-4 appeared more porous with lower indexing rates over the whole region-quantification of this porosity is currently a work in progress. It is important to recall that images at each site were collected at different image resolutions, allowing for maximum efficiency and coverage whilst maintaining the high indexing ratios (Table 1). As some grains were smaller than the specified step-size for imaging each site, this may have resulted in non-indexing of those grains, making the EBSD-inferred porosity of the region incorrect. In light of this, secondary electron images were obtained (Supplementary Fig. 5) for each matrix site, and these confirmed and qualified the porosity variations implied in the EBSD maps.

### 3.3. Slip systems

Based upon the misorientation axes observed from the EBSD maps we have inferred the likely slip-systems that have contributed to the LABs in chondrules, AOA grains and matrix grains including those within the TKD data. C-1 and C-3 had a misorientation axis of the [100] ($a$-axis), while C-2 had misorientation along the [010] ($b$-axis) (Fig. 8). Matrix grains largely had misorientation axes of [010] ($b$-axis) whilst one examined grain at M-3 had a misorientation axis of [100] ($a$-axis). EBSD, BSE and SE images indicated that the LABs occur within grains and so it was assumed they result from intragrain plasticity, which would have required high stresses. Chondrule site C-3 (Fig. 7c) displayed evidence of two different slip systems; the misorientation axis was [100] in both cases, but one slip system comprised slip in the [001] direction along the (010) plane, and the other involved slip in the [010] direction along the (001) plane. A variety of slip systems were inferred across each of the sites; of the 9 examples found, matrix slip systems were most commonly (001)[100] (slip in the (001) direction along the [100] plane), with occurrences of other common systems at each site. Chondrule grain slip systems were more widely varied and include (001)[010], (001)[100] and (010)[100] throughout the sites.

### 3.4. Strain distribution observations

The qualitative distribution of strain observed in chondrules and matrix is consistent with numerical simulations results (Fig. 9). In the simulated chondrules, the predicted mean strain is low, but localised near their margins for 1.0 and 1.5 km/s cases (Figs. 9a and b), whereas strain is higher and distributed throughout the chondrules for the 2 km/s case (Fig. 9c). In all simulated impactor velocity scenarios, the matrix strain is always higher than within the chondrules, with an increase in mean strain with impactor velocity (Fig. 9). Strain in the matrix is typically more intensely developed immediately adjacent to the chondrules, most commonly with an eccentric distribution and asymmetric strain shadows (Fig. 9). All of the simulations predict strong gradients in matrix strain over the micrometre scale (Fig. 9).

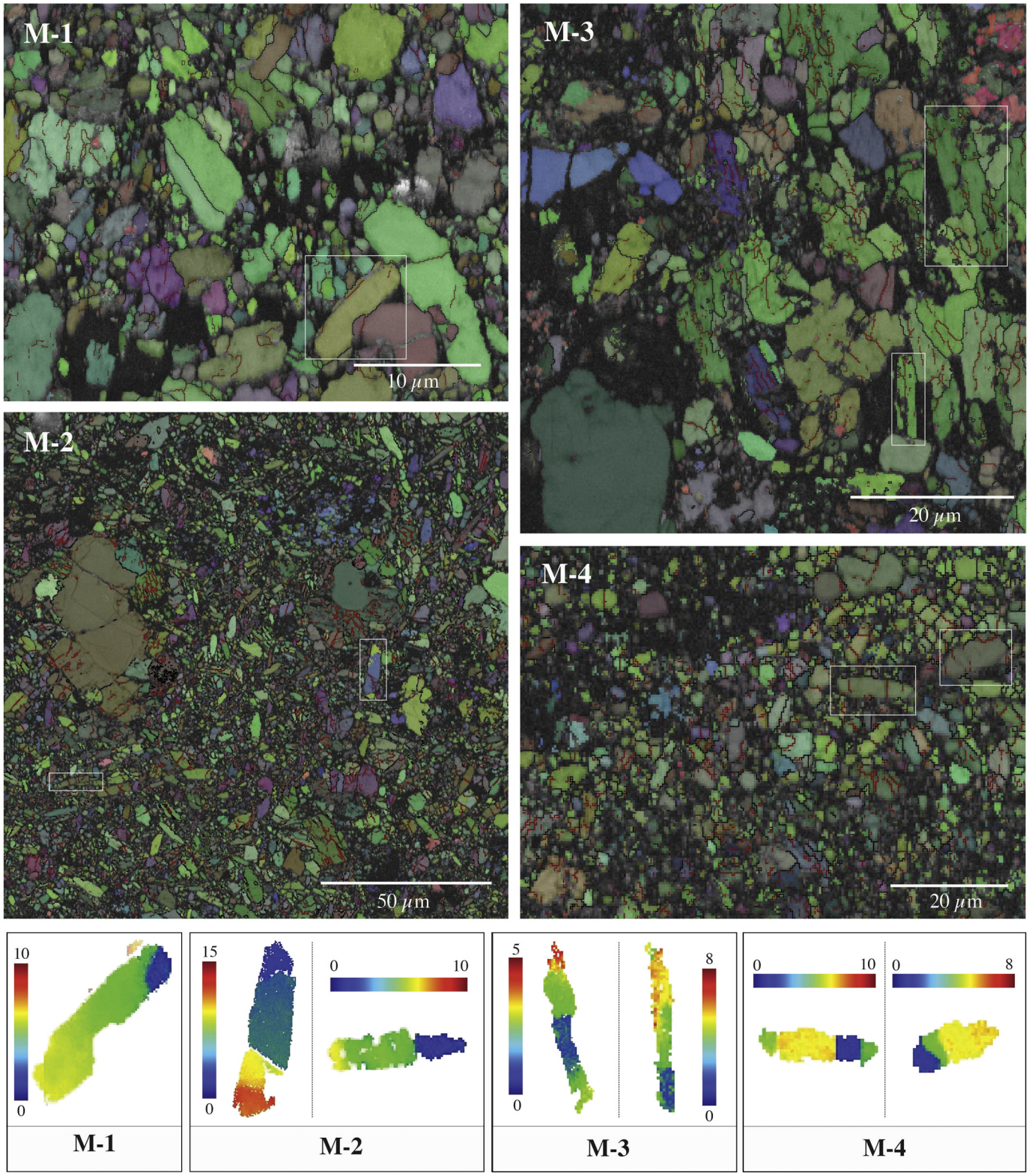


**Fig. 5.** Four matrix sites (M-1–4) shown using Euler maps. White boxes in each image refer to laths displayed in lower panel; texture maps of individual grains demonstrate the extent of deformation that has occurred throughout the full length of the grain. Scale bar shows degrees (°) of deformation from pre-defined unstrained point of grain (blue region).

## 4. Discussion

Previous work has shown that Allende has a weak but prominent fabric throughout, with an alignment of the short < 100 > axis of fayalitic olivine grains (Watt et al., 2006). Our study confirmed the weak fabric, albeit with varying alignments (Supplementary Figs. 1–4 and 6). Chondrules, AOAs, CAIs and larger grains are elongate in the vertical orientation, indicative of a horizontal compaction orientation in the plane of the images (Fig. 1). However, we also observed a significant difference in spatial distri-

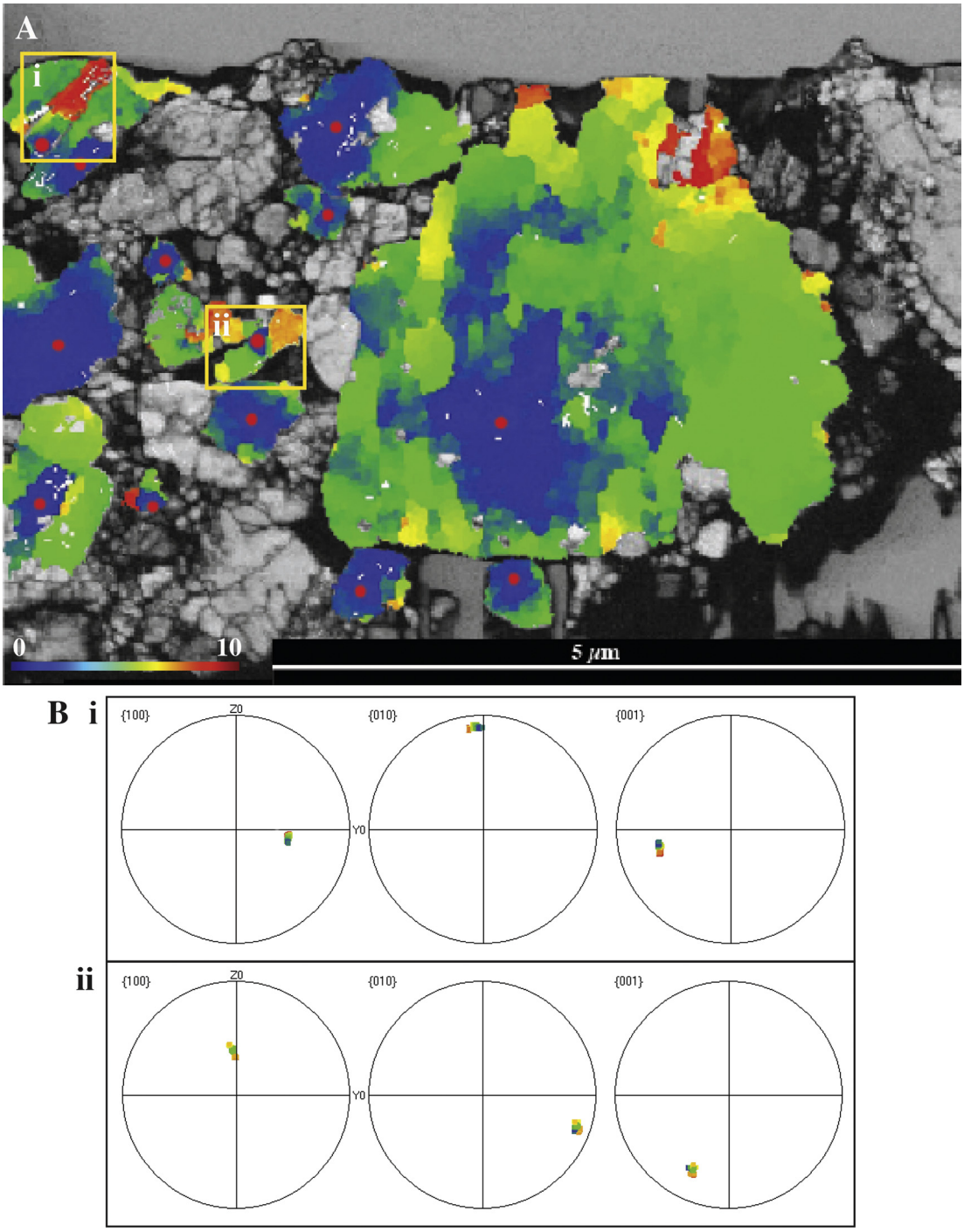


**Fig. 6.** EBSD image of a TKD section of Allende (A). Greyscale image is the band contrast map, indicating the quality of the patterns obtained in imaging by the brightness of the colours (i.e. white/light greys = good band contrast and pattern quality). Colour overlay demonstrates the amount of crystallographic orientation deviation in degrees from user-defined reference points (red dots) in selected grains. Lower-hemisphere, equal area plots show dispersion of each crystallographic axis within the grain (B).

bution and density of deformation between chondrule and matrix olivines: an absence of deformation of chondrule interiors, minor crystal-plastic deformation at the edges of chondrule grains (up to 6° misorientation ductile strain in the outer 20 μm of these grain edges), and moderate yet heterogeneous crystal-plastic deformation throughout matrix grains (e.g., 20° misorientation along the length of a 20 μm grain). The low-angle boundaries in the matrix grains also have a preferential alignment (their traces are vertical in the plane of the images) whereas those in the chondrules rims are generally parallel to the edge of the grains (Fig. 7).

A large portion of the deformation of chondrule grain edges is concentrated at the top, bottom and to the right of the chondrules. Further to this, deformation is absent on the left and less prominent on the right of these grains when compared with the top and bottom areas. Coupled with an absence of matrix grain deformation to the left of such grains, a compressional 'shadow' has been generated. It is possible that compaction of pores against the boundary of the grain normal to the compacting direction generated enough heat such that these areas of the grains were compressed but show no evidence of strain. The top and bottom of the

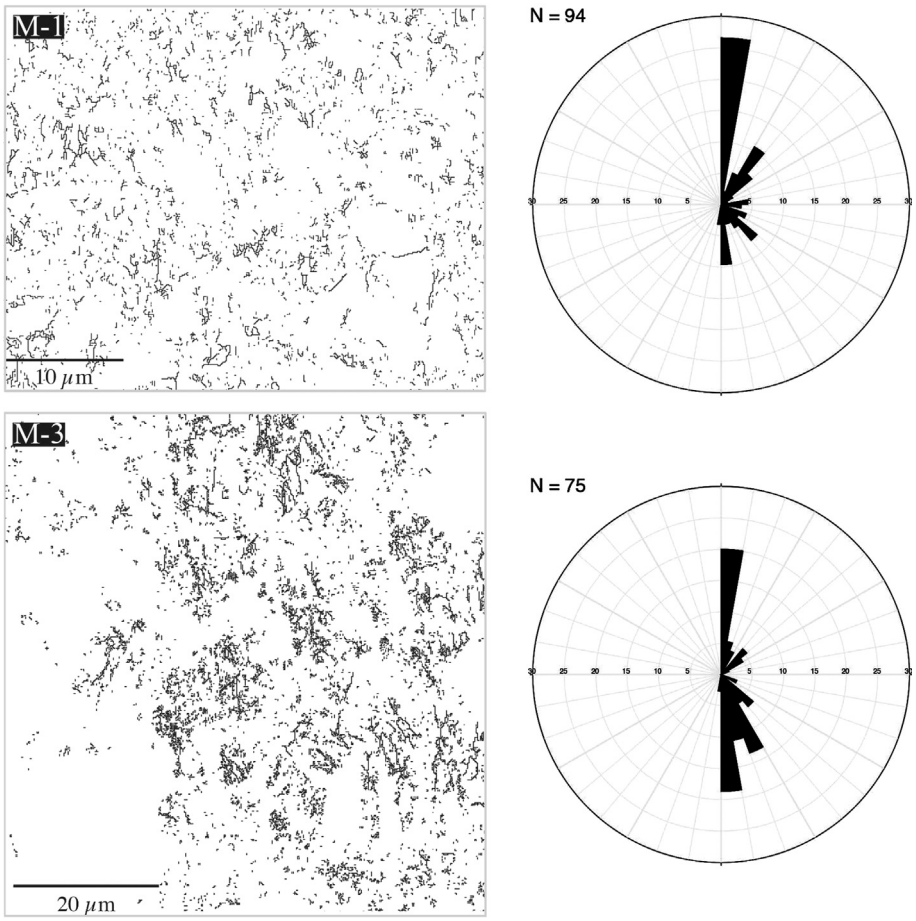


**Fig. 7.** Low-angle boundaries (1°–10°) are presented for matrix sites M-1 and M-3 on the left. The orientations of these boundaries are plotted onto rose diagrams on the right, demonstrating the preferential orientation for both sites is roughly N–S, or at 0° and 180°.

chondrules may not have experienced the same degree of compaction and, therefore, less pore collapse and subsequent heating would have occurred (Davison et al., 2010). Here, there may not have been sufficient heat to deform these regions without strain being evident. However, the lack of evidence for melting observed at this scale indicates this may not be the case, and therefore other possibilities, such as shear heating, should be considered. Given that the presence of strain 'shadows' on the left side of the larger grains, it is probable that a similar shadow would be evident in the matrix as a higher porosity relative to surrounding matrix areas. Whilst the sample has lost a large portion of it's initial porosity (∼50%), the compaction process is very unlikely to generate uniformly low porosities throughout the matrix due to the bimodal grain size distribution of the material, and therefore porosity heterogeneities are to be expected.

The microstructural analysis clearly shows that deformation was spatially heterogeneous, and indicative that Allende experienced locally heterogeneous (stress, temperature) conditions. Olivine deforms crystal-plastically in response to stress at high temperatures. This is achieved by the activity of several possible dislocation slip systems, and it is well established that distinct slip systems operate in different environmental conditions (e.g. stress, temperature, $H_2O$ activity) for terrestrially deformed olivine (Karato et al., 2008). Operation of different slip systems produces different types of crystallographic fabric, which can be identified by trends in clustering in lower-hemisphere, equal-area plots of the EBSD data (Karato et al., 2008). Therefore, quantification of fabrics may be used to infer temperature and pressure conditions at the time of fabric generation. Using this approach, we can deduce that the variable slip-systems identified within the chondrules and AOA probably reflected heterogeneous stress and temperature conditions throughout the sample. Most slip systems within matrix grains are indicative of deformation under dry and low-moderate stress conditions, with some variation to higher-stress slip systems (Karato et al., 2008). M-1 and M-2 presented a weak A-type fabric when compared with Karato et al.'s (2008) classification system, where M-3 displayed a D-type fabric. The fabric types indicated high temperatures (>1470 K) and low stresses (0–350 MPa) at sites M-1 and M-2, and moderate temperature (1200–1470 K) and stress (>350 MPa) conditions at M-3 (Karato et al., 2008). Sites M-1 and M-2 were situated away from chondrules, whereas M-3 was very close to and between two chondrules and so higher stresses may be expected. However, the lack of high-pressure phases and mosaicism of LABs in the sample limit the shock pressures at time of deformation to below 10 GPa (Langenhorst, 2002). There has been some speculation that the presence of pores prior to compaction allows for higher-temperature slip-systems to activate in olivine when compared with zero-porosity samples (Goetze and Poirier, 1978). Therefore, it is possible that higher-temperature slip-systems may have activated in highly porous regions of the sample.

The microstructures observed in this sample of Allende and other evidence can be used to evaluate several different models for the compaction of Allende. An early theory highlighted a static force, such as burial compaction due to gravity, as a possible source of compression (Fujimara et al., 1983). The microstructural features we have observed in this study do not indicate that this is the compaction mechanism; the asymmetry in large grain deformation

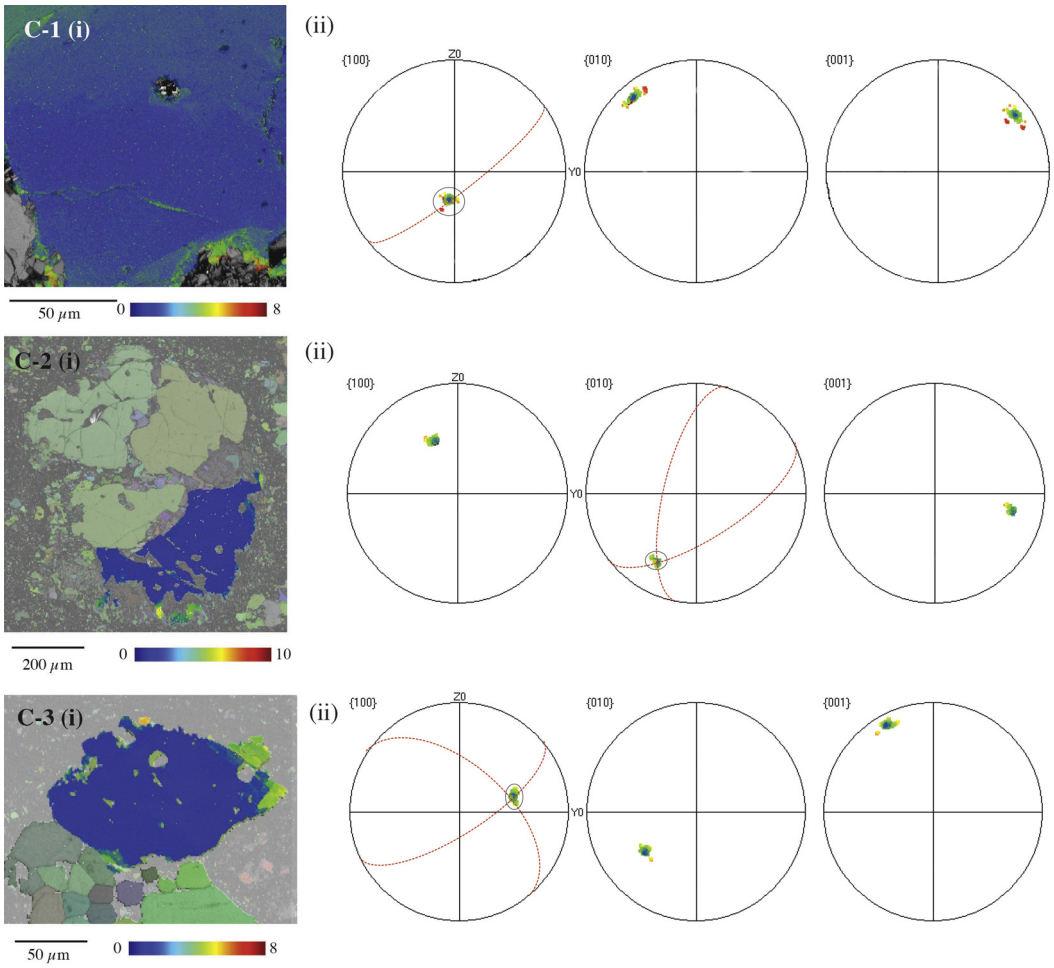


**Fig. 8.** Texture component maps of Chondrule/AOA site C-1, C-2 and C-3 (i). This demonstrates the degrees of rotation in Euler angles from a central, unstrained point within the presented grain. This data is plotted on lower hemisphere, equal area, stereographic projections (ii). At each site the orientation of the low-angle boundaries is shown on the equal area plots as red lines for each highlighted grain in the maps. At site C-1 and C-3, the misorientation axis is the [100] axis, and at C-2 the misorientation axis is [010]. At sites C-2 and C-3 two sets of low-angle boundaries are observed and cause a two-way dispersion in the data.

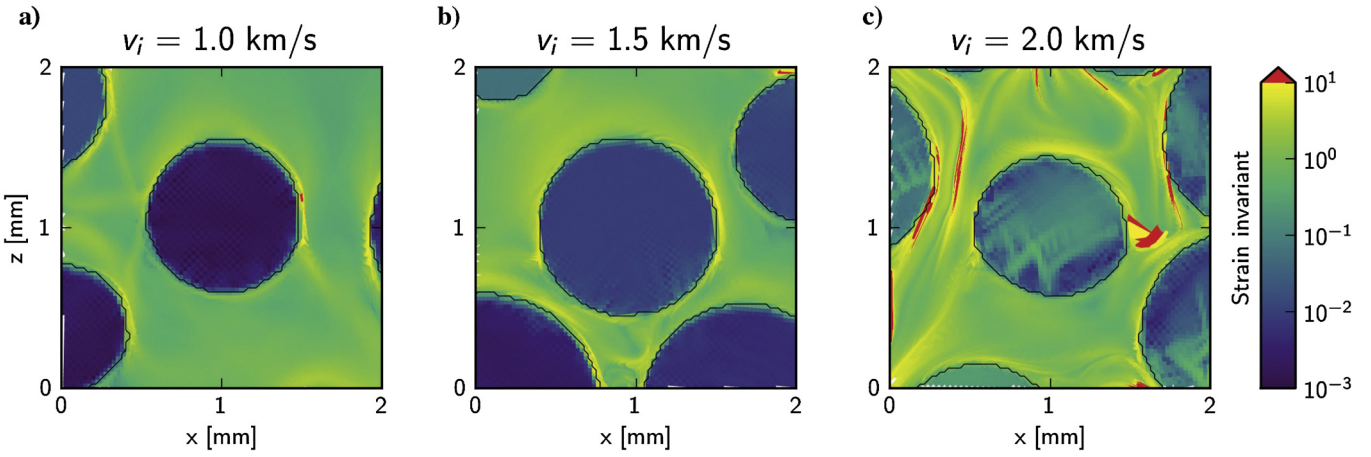


**Fig. 9.** Finite invariant shear strain distribution maps derived from numerical simulations for three impact speeds: a) $v = 1.0$ km/s; b) 1.5 km/s; c) 2.0 km/s, which generate bulk shock pressures of approximately 1, 1.7 and 3 GPa, respectively. In these simulations chondrules are treated as single grains and the matrix of fine grains and pore space is treated as a continuum. Hence, while simulated strains in the chondrules are expected to be comparable to those observed inside chondrule grains, the strain distribution within the matrix is the bulk strain of both matrix grains and pore space combined and is not directly comparable to strain observed in individual matrix grains.

indicates localised compaction from one direction, not multiple directions. The slip systems that activated within the grains are widely varied, but some require heating beyond 1450 °C; in the case of lithostatic compaction, heating is expected to be continuous for the duration of the slow compaction process as pores are continuously destroyed. If temperatures of 1450 °C were achieved for any length of time, widespread melting would have occurred, which has not been observed. A lack of overprinting in the mi-

crostructures also implies all structural features were generated at the same time; compaction due to lithostatic forces would result in microstructures forming over longer time periods, and therefore we might expect to see cross-cutting deformation relationships. At a larger scale, Allende's tensile strength is approximately 28 MPa in its currently compressed form (Svetsov et al., 1995). This strength may be surpassed in the centre of a planetary body with a radius greater than approximately 300 km and, therefore, lithostatic pressure may result in the compaction observed if Allende sampled the centre of a planetary body. However, this mechanism is unable to explain the asymmetry of deformation in the chondrules and distribution of porosity and crystal-plasticity in the matrix grains. Porosity reduction under these conditions should have orthorhombic symmetry. Overburden-related stresses in small planetary bodies are unlikely to be high enough to activate slip systems responsible for the observed fabrics in the matrix olivine in Allende. Furthermore, Allende is a primitive meteorite of petrologic type 3, and if it originates from the centre of a planetary body, it would not remain in a primitive state. A number of CO, CR and CM meteorites have lower porosities than Allende (Macke et al., 2011), and so if the same principle applies to their deep origin on their respective parent bodies, many asteroids would have been completely destroyed to create a number of meteorites in our collections. The oxidised CV subclass (e.g. Allende) is significantly less compacted than the reduced CV subclass (20% porosity compared with ~5% porosity) (Macke et al., 2011), but the oxidised samples present significantly higher metamorphism. We would expect the inverse relationship to be evident where lithostatic overburden forces are dominant. There are currently asteroids in our solar system that appear to be of low bulk density when compared with their likely meteorite equivalents (Britt et al., 2002); this suggests that these bodies are still highly porous, and so a planet-wide compaction process is further unlikely. Gravitational compressional forces generate gradual and continuous heating and were likely involved in the early heating of the body and initial stages of lithification. Therefore, we believe that it is improbable that lithostatic overburden could have generated the compressional microstructures, but possibly contributed to overall lithification.

Consequently, we consider the case of dynamic and rapid compressional forces during impact events in the creation of the aforementioned microstructures. The asymmetric distribution of strain (i.e., crystal-plastic deformation and porosity reduction) around chondrules and AOA grains, and highly heterogeneous stresses and temperatures inferred from operative slip systems are consistent with numerical simulations of impacts at these scales (Davison et al., 2010; 2014; Bland et al., 2014). We observed a varied yet generally greater intensity of deformation in small matrix grains when compared with large chondrule and AOA grains; given a rapid loss of pore space upon compaction generates a temperature increase, the matrix would likely experience more heat than chondrules, and consequently would be more deformed relative to the large low-porosity grains. The preferential orientation of LAB planes and crystallographic preferred orientation in the matrix grains can be readily explained by differential heating between chondrules and matrix during a single moderate-strong impact event, which would consequently reduce bulk porosity. Microstructural evidence also indicates an instantaneous and rapid compressional force is responsible.

Allende has a lack of macrostructure shock features that previously suggested it was unaffected by impact, however as a result of porosity loss, any further impacts post-compaction are unlikely to cause substantial compression or generate compaction-related shock features (Sharp and DeCarli, 2006; Davison et al., 2010; Bland et al., 2014). Compaction via impact is a much simpler scenario when compared with lithostatic overburden; it is unlikely that a large number of asteroids were completely destroyed to produce the samples in our vast meteorite collections, and low-velocity collisions into small planetary bodies are much more common and easier to achieve (Housen and Holsapple, 2011; Beitz et al., 2013). At a planetary scale, samples originating closer to the asteroid surface would show more evidence of metamorphism when compared with samples at depth on the parent body following impact processing; this is reflected in the properties of oxidised and reduced CV class meteorites, where higher porosities and significant metamorphism are observed in oxidised samples compared with reduced samples. *In situ* evidence of impacts into highly porous bodies has been found on C-type asteroid Mathilde; whilst CV meteorites may not originate from C-type asteroids (Bell, 1988), the principal of impacts into early, highly porous bodies is well supported by this prior research (Housen et al., 1999; Cheng and Barnouin-Jha, 1999; Housen and Holsapple, 2011). Furthermore, conclusions from impact compaction studies that correlate compaction pressures with overall shock stages for each carbonaceous chondrite class support our findings (Weidenschilling and Cuzzi, 2006; Beitz et al., 2013).

Shock wave attenuation into a polymineralic and porous media has been shown to induce shear heating at grain boundary contacts (Gillet and Goresy, 2013). We predict Allende to have experienced no more than 10 GPa based on the absence of high-pressure polymorphs and mosaicism in the olivine grains. At this pressure, we expect that Allende would have begun to melt at 1600 °C, but at lower pressures heating to 1150 °C could have induced melting (Agee et al., 1995). The microstructural features presented indicate that these grains did not experience such temperatures, but shear heating may have been more pronounced at the grain boundaries, resulting in grain sintering, lithification and strengthening of Allende. The geometry of deformation seen in the matrix does show potential evidence of shear processing (Fig. 5), whereby LABs parallel to the direction of compression have formed. Additionally, the lower edges of C-1 and C-3 (Fig. 2) appear fragmented from the rest of the surrounding material, which could indicate that shear-induced disaggregation has occurred. Experiments examining the sintering behaviour of olivine have found that it is favoured where a fine-grained (micrometre-scale) aggregate is rapidly heated to high $T$: an analogous scenario to that encountered by a high porosity matrix during impact-induced compaction (Cooper and Kohlstedt, 1984). Weak evidence of this can be found in Allende (Fig. 6), where grains have a higher amount of deformation at their contact margin. However, understanding the intricacies of lithification in this sample is beyond the scope of this paper and should be examined at higher resolution in future work.

The local and regional pressure and temperature anomalies over distances of 10–100 μm can be attributed to interactions of shock waves in the bimodal, porous medium, resulting in heterogeneous deformation. The simulations described by Bland et al. (2014) reveal that low-velocity impacts of 2 km/s in a material of 70% matrix, 30% chondrule result in peak pressures in chondrules of ≈6.5 GPa, but with predicted post-shock heating temperatures of 370 K in chondrules, and 1100 K in the matrix. These models also yield large disparities in peak pressure between matrix and chondrules; chondrule interiors realistically experience 4–5 GPa, chondrule edges approximately up to 8 GPa, and over only 100 μm within the matrix, a pressure range of 7–18 GPa may arise (Bland et al., 2014). Whilst peak pressures cannot be directly compared with our data, comparisons with the modelled first order approximations of corresponding strain distribution are more analogous. Acknowledging the limitations of the simulations to be able to capture the complexity of olivine rheology exactly, the strain in the modelled 1.0 km/s and 1.5 km/s scenarios (<2 GPa bulk shock pressure) show the strongest similarity to the observed chondrule deformation from EBSD mapping (Figs. 2, 3 and 4). First-order predictions of the higher intensity strain in the matrix are also

consistent with observations from EBSD mapping (Figs. 5 and 6). These outcomes suggest the modelling accurately predicts the response of a bimodal sample to compression and we infer impacts are responsible for the petrographic features described.

## 5. Conclusions

EBSD analysis in this study of Allende has revealed the following:

1. Crystal-plastic deformation at the margins of chondrule grains, commonly with an asymmetric distribution (in the context of all figures shown).
2. A lack of crystal-plastic deformation within chondrule interiors ($<1°$).
3. High degrees of crystal-plastic deformation throughout matrix olivine grains (up to 20° of misorientation). This deformation was spatially heterogeneous, with asymmetric zones of intense deformation close to chondrules.
4. A dominance of LABs in matrix olivine grains with strongly preferred boundary plane orientations in the reference frame of the sample surface.

We conclude Allende has been compacted via impact processing. Planar shock modelling shows a low impact velocity of a few km/s into a 50% bulk porosity target material is sufficient to produce the features present. The effect of the temperature difference between the two components following impact is large and significant; however, such expected low pressures (1–1.3 GPa, Bland et al., 2014) are unlikely to have produced petrographic shock evidence traditionally observed in chondrules. Matrix grains are the key to understanding the magnitude of the compaction-inducing impact, as they show preservation of compaction-related deformation and provide a more accurate representation of peak temperatures and stresses.

## Acknowledgements

This work was funded by the Australian Research Council via their Australian Laureate Fellowship programme (FL110100074) (PAB). This research was supported by the Curtin International Postgraduate Research Scholarship awarded to LF and LD, and GKB acknowledges support from Curtin University via their Research Fellowship scheme. GSC and TMD acknowledge funding from the UK Science and Technology Facilities Council STFC grant ST/J001260/1. The authors would also like to acknowledge the technical assistance and use of facilities at John de Laeter Microscopy centre, at Curtin University; the Australian Synchrotron XFM beamline, and the University of Sydney node of the Australian Microscopy & Microanalysis Research Facility: Sydney Microscopy & Microanalysis. The authors would like to thank the handling editor and anonymous reviewer for their constructive comments in the review process.

## Appendix A. Supplementary material

Supplementary material related to this article can be found online at http://dx.doi.org/10.1016/j.epsl.2016.07.050.

## References

Agee, C.B., Li, J., Shannon, M.C., Circone, S., 1995. Pressure-temperature phase diagram for the Allende meteorite. J. Geophys. Res., Solid Earth (1978–2012) 100 (B9), 17725–17740.

Bland, P.A., Howard, L.E., Prior, D.J., Wheeler, J., Hough, R.M., Dyl, K.A., 2011. Earliest rock fabric formed in the solar system preserved in a chondrule rim. Nat. Geosci. 4 (4), 244–247.

Bland, P.A., Collins, G.S., Davison, T.M., Abreu, N.M., Ciesla, F.J., Muxworthy, A.R., Moore, J., 2014. Pressure–temperature evolution of primordial solar system solids during impact-induced compaction. Nat. Commun. 5, 5451.

Beitz, E., Guettler, C., Nakamura, A.M., Tsuchiyama, A., Blum, J., 2013. Experiments on the consolidation of chondrites and the formation of dense rims around chondrules. Icarus 225 (1), 558–569.

Bell, J.F., 1988. A probable asteroidal parent body for the CO or CV chondrites. Meteoritics 23, 256–257.

Blum, J., 2003. The structure of planetesimals in the solar nebula (abstract #5152). Meteorit. Planet. Sci. 38 (Suppl.), A83.

Bowling, T.J., 2015. Global surface modification of asteroid 4 Vesta following the Rheasilvia impact. PhD thesis. Purdue University.

Brenker, F.E., Palme, H., Klerner, S., 2000. Evidence for solar nebula signatures in the matrix of the Allende meteorite. Earth Planet. Sci. Lett. 178, 185–194.

Britt, D.T., Yeomans, D., Housen, K., Consolmagno, G., 2002. Asteroid density, porosity, and structure. In: Asteroids III.

Cain, P.M., McSween, H.Y., Woodward, N.B., 1986. Structural deformation of the Leoville chondrite. Earth Planet. Sci. Lett. 77, 165–175.

Cheng, A.F., Barnouin-Jha, O.S., 1999. Giant craters on Mathilde. Icarus 140 (1), 34–48.

Consolmagno, G.J., Britt, D.T., Stoll, C.P., 1998. The porosities of ordinary chondrites: models and interpretation. Meteorit. Planet. Sci. 33 (6), 1221–1229.

Cooper, R.F., Kohlstedt, D.L., 1984. Sintering of olivine and olivine-basalt aggregates. Phys. Chem. Miner. 11 (1), 5–16.

Cuzzi, J.N., Weidenschilling, S.J., 2006. Particle-gas dynamics and primary accretion. In: Lauretta, D.S., McSween Jr., H.Y. (Eds.), Meteorites and the Early Solar System II. Univ. of Arizona, Tucson, pp. 353–381.

Cuzzi, J.N., Hogan, R.C., Shariff, K., 2008. Toward planetesimals: dense chondrule clumps in the protoplanetary nebula. Astrophys. J. 687, 1432.

Davison, T.M., Collins, G.S., Ciesla, F.J., 2010. Numerical modelling of heating in porous planetesimal collisions. Icarus 208 (1), 468–481.

Davison, T.M., Collins, G.S., Bland, P.A., 2014. Mesoscale numerical modelling of compaction of primitive solar system solids in low-velocity collisions. In: 45th Lunar and Planetary Science Conference. Abstract #2718.

Dyl, K.A., Cleverley, J.S., Bland, P.A., Ryan, C.G., Fisher, L., Hough, R.M., 2014. Quantified, whole section trace element mapping of carbonaceous chondrites by synchrotron X-ray fluorescence microscopy: 1. CV meteorites. Geochim. Cosmochim. Acta 134 (4), 1176–1180.

Fisher, L.A., Fougerouse, D., Cleverley, J.S., Ryan, C.G., Micklethwaite, S., Halfpenny, A., Hough, R., Gee, M., Paterson, D., Howard, D.L., Spiers, K., 2014. Quantified, multi-scale X-ray fluorescence element mapping using the Maia detector array: application to mineral deposit studies. Miner. Depos. 50 (6), 665–674.

Fliervoet, T.F., Drury, M.R., Chopra, P.N., 1999. Crystallographic preferred orientations and misorientations in some olivine rocks deformed by diffusion or dislocation creep. Tectonophysics 303 (1), 1–27.

Friedrich, J.M., Rubin, A.E., Beard, S.P., Swindle, T.D., Isachsen, C.E., Rivers, M.L., Macke, R.J., 2014. Ancient porosity preserved in ordinary chondrites: examining shock and compaction on young asteroids. Meteorit. Planet. Sci. 49 (7), 1214–1231.

Fujimara, A., Kato, M., Kamazawa, M., 1983. Preferred orientation of phyllosilicate (001) in matrix of Murchison meteorite and possible mechanisms of generating the oriented texture in chondrites. Earth Planet. Sci. Lett. 66, 25–32.

Gattacceca, J., Rochette, P., Denise, M., Consolmagno, G., Folco, L., 2005. An impact origin for the foliation of chondrites. Earth Planet. Sci. Lett. 234 (3), 351–368.

Gillet, P., Goresy, A.E., 2013. Shock events in the solar system: the message from minerals in terrestrial planets and asteroids. Annu. Rev. Earth Planet. Sci. 41, 257–285.

Goetze, C., Poirier, J.P., 1978. The mechanisms of creep in olivine [and discussion]. Philos. Trans. R. Soc., Math. Phys. Eng. Sci. 288 (1350), 99–119.

Gray, E.M., 2013. Deformation of Earth's upper mantle: insights from naturally occurring fabric types. Diss. PhD thesis. Curtin University, 327 pp.

Hanna, R.D., Ketcham, R.A., Zolensky, M., Behr, W.M., 2015. Impact-induced brittle deformation, porosity loss, and aqueous alteration in the Murchison CM chondrite. Geochim. Cosmochim. Acta 171, 256–282.

Housen, K.R., Holsapple, K.A., Voss, M.E., 1999. Compaction as the origin of the unusual craters on the asteroid Mathilde. Nature 402 (6758), 155–157.

Housen, K.R., Holsapple, K.A., 2011. Ejecta from impact craters. Icarus 211 (1), 856–875.

Johansen, A., Youdin, A., Mac Low, M.-M., 2009. Particle clumping and planetesimal formation depend strongly on metallicity. Astrophys. J. Lett. 704 (2), L75–L79.

Karato, S., Haemyeong, J., Katayama, I., Skemer, P., 2008. Geodynamic significance of seismic anisotropy of the upper mantle: new insights from laboratory studies. Annu. Rev. Earth Planet. Sci. 36, 59–95.

Kohlstedt, D.L., Goetze, C., 1974. Low-stress high-temperature creep in olivine single crystals. J. Geophys. Res. 79 (14), 2045–2051.

Langenhorst, F., 2002. Shock metamorphism of some minerals: basic introduction and microstructural observations. Bull. Czech Geol. Surv. 77 (4), 265–282.

Macke, R.J., Britt, D.T., Consolmagno, G.J., 2011. Density, porosity, and magnetic susceptibility of achondritic meteorites. Meteorit. Planet. Sci. 46 (2), 311–326.

McSween Jr., H.Y., 1979. Are carbonaceous chondrites primitive or processed? A review. Rev. Geophys. Space Phys. 17 (1059), 1075.

Nakamura, T., Tomeoka, K., Takeda, H., 1992. Shock effects of the Leoville CV carbonaceous chondrite: a transmission electron microscope study. Earth Planet. Sci. Lett. 114, 159–170.

Rubin, A., 2004. Postshock annealing and postannealing shock in equilibrated ordinary chondrites: implications for the thermal and shock histories of chondritic asteroids. Geochim. Cosmochim. Acta 68 (3), 673–689.

Scott, E.R.D., Keil, K., Stöffler, D., 1992. Shock metamorphism of carbonaceous chondrites. Geochim. Cosmochim. Acta 56 (12), 4281–4293.

Scott, E.R.D., 2002. Meteorite evidence for the accretion and collisional evolution of asteroids. In: Bottke, W.F., et al. (Eds.), Asteroids III. Univ. of Arizona, Tucson, pp. 697–709.

Sharp, T.G., DeCarli, P.S., 2006. Shock effects in meteorites. In: Lauretta, D.S., McSween Jr., H.Y. (Eds.), Meteorites and the Early Solar System II. Univ. Arizona Press, pp. 653–677.

Stacey, F.D., Lovering, J.F., Parry, L.G., 1961. Thermomagnetic properties, natural magnetic moments, and magnetic anisotropies of some chondritic meteorites. J. Geophys. Res. 66, 1523–1534.

Stöffler, D., Keil, K., Scott, E., 1991. Shock metamorphism of ordinary chondrites. Geochim. Cosmochim. Acta 55 (12), 3845–3867.

Svetsov, V.V., Nemtchinov, I.V., Teterev, A.V., 1995. Disintegration of large meteoroids in Earth's atmosphere: theoretical models. Icarus 116 (1), 131–153.

Trimby, P.W., Cao, Y., Chen, Z., Han, S., Hemker, K.J., Lian, J., Liao, X., Rottmann, P., Samudrala, S., Sun, J., Wang, J.T., Wheeler, J., Cairney, J.M., 2014. Characterizing deformed ultrafine-grained and nanocrystalline materials using transmission Kikuchi diffraction in a scanning electron microscope. Acta Mater. 62, 69–80.

Watt, L., Bland, P.A., Prior, D.J., Russell, S.S., 2006. Fabric analysis of Allende matrix using EBSD. Meteorit. Planet. Sci. 41, 989–1001.

Weidenschilling, S.J., Cuzzi, J., 2006. Accretion dynamics and timescales: relation to chondrites. In: Lauretta, D.S., McSween Jr., H.Y. (Eds.), Meteorites and the Early Solar System II. Univ. Arizona Press, pp. 473–485.

Wheeler, J., Reddy, S.M., Cliff, R.A., 2001. Kinematic linkage between internal zone extension and shortening in more external units in the NW Alps. J. Geol. Soc. 158 (3), 439–443.

Zolensky, M.E., Mittlefehldt, D.W., Lipschutz, M.E., Wang, M.S., Clayton, R.N., Mayeda, T.K., Grady, M.M., Pillinger, C., Barber, D., 1997. CM chondrites exhibit the complete petrologic range from type 2 to 1. Geochim. Cosmochim. Acta 61, 5099–5115.